AAAS
Research
Volume 2019, Article ID 6930294, 9 pages
https://doi.org/10.34133/2019/6930294

Research
OFFICIAL JOURNAL OF CAST

Research Article

High Capacity and Superior Rate Performances Coexisting in Carbon-Based Sodium-Ion Battery Anode

Yuqian Li[1], Liyuan Zhang[1], Xiuli Wang[1], Xinhui Xia[1], Dong Xie[2], Changdong Gu[1], and Jiangping Tu[1]

[1]*State Key Laboratory of Silicon Materials, Key Laboratory of Advanced Materials and Applications for Batteries of Zhejiang Province, School of Materials Science and Engineering, Zhejiang University, Hangzhou 310027, China*
[2]*Guangdong Engineering and Technology Research Center for Advanced Nanomaterials, School of Environment and Civil Engineering, Dongguan University of Technology, Dongguan 523808, China*

Correspondence should be addressed to Xiuli Wang; wangxl@zju.edu.cn, Xinhui Xia; helloxxh@zju.edu.cn, and Jiangping Tu; tujp@zju.edu.cn

Received 26 March 2019; Accepted 6 June 2019; Published 25 June 2019

Copyright © 2019 Yuqian Li et al. Exclusive Licensee Science and Technology Review Publishing House. Distributed under a Creative Commons Attribution License (CC BY 4.0).

Amorphous carbon is considered as a prospective and serviceable anode for the storage of sodium. In this contribution, we illuminate the transformation rule of defect/void ratio and the restrictive relation between specific capacity and rate capability. Inspired by this mechanism, ratio of plateau/slope capacity is regulated via temperature-control pyrolysis. Moreover, pore-forming reaction is induced to create defects, open up the isolated voids, and build fast ion channels to further enhance the capacity and rate ability. Numerous fast ion channels, high ion-electron conductivity, and abundant defects lead the designed porous hard carbon/Co_3O_4 anode to realize a high specific capacity, prolonged circulation ability, and enhanced capacity at high rates. This research deepens the comprehension of sodium storage behavior and proposes a fabrication approach to achieve high performance carbonaceous anodes for sodium-ion batteries.

1. Introduction

Recently, many alternatives of lithium-ion batteries (LIBs), which are restricted by the rising costs, are investigated to satisfy the demand of energy storage. Particularly, sodium-ion batteries (SIBs) are widely researched due to (1) abundant resource (23600 ppm in the earth crust, 1000 times more than lithium) and the even distribution of sodium, (2) low cost of sodium, and (3) similar physicochemical properties to lithium [1–3]. Therefore, the successful experience of cathode for LIBs might be copied to SIBs firsthand [4, 5]. Unfortunately, some decent-performance anodes of LIBs in current research, such as Sn [6], Si [7], and their alloys, titanium-based salts [8], and metal oxides/sulfides/phosphides or their analogues (Fe_3O_4 [9], MnO [10], Mn_3O_4 [11], Co_3O_4 [12, 13], SnO_2 [14], $CoSe_2$ [15], CoS_2 [16], MoS_2 [17–19], and Sn_4P_3 [20]), are problematic in SIBs. Hence, it is of great significance to develop suitable anodes for SIBs.

Graphite is the promising and competitive anode for LIBs. Nevertheless, it has not exhibited equivalent performance for SIBs, which is probably due to the larger radius of Na^+ [21, 22]. At present, kinds of other amorphous carbonaceous materials that possess large interlayer distance and disordered structure have been developed as anodes for SIBs. Hard carbon (HC), including heteroatom-doped hard carbon [7, 23, 24] and biomass-derived carbon [25–31], exhibits strong competitiveness. These amorphous carbon materials can insert/extract sodium ions at a low voltage [25, 32–34].

Amorphous carbon exhibits distinct behaviors of sodium storage at different voltages. Thereby, the charge-discharge curve can be divided into slope and plateau segments. There are diverse explanations for the sodium-ion storage behavior of amorphous carbon: insertion-absorption, absorption-insertion, and absorption-filling mechanisms [35]. Among them, absorption-filling mechanism is widely verified [28, 36–38], which means the following: (1) defects, fringes, and the surface among the regional graphitizing area contribute to the slope capacity; (2) nanodomains and nanovoids are ascribed to the reserve of sodium ions in the plateau capacity [39–42].

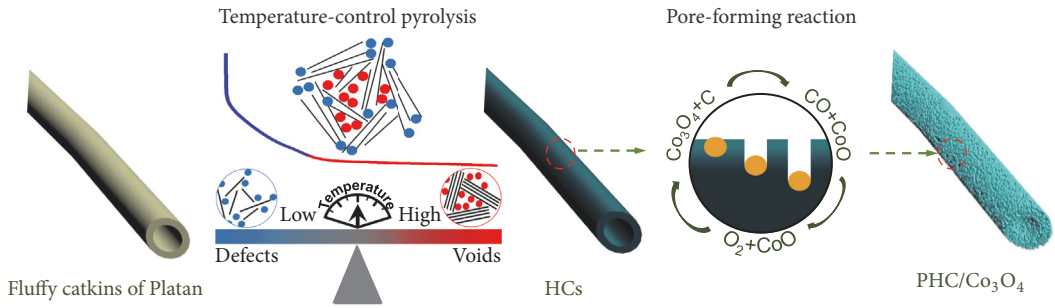


Figure 1: General diagram of the preparation process and formation mechanism of PHC/Co_3O_4.

Inspired by this mechanism, HC can be modified via the following routines: (1) increasing defects and edges to improve the slope capacity, (2) creating more domains and voids to enhance the plateau capacity, and (3) constructing fast sodium-ion channel. Thus, optimal performance can be realized by regulating the ration of slope and plateau region. On one hand, different carbonization temperature can adjust the graphitization degree of carbon, and thereby the ratio of slope region and plateau region is controllable [28, 43, 44]. On the other hand, the pore-forming process can create more voids and build fast sodium-ion channels. Chemical activating reagent (such as KOH [45, 46] and HNO_3 [45]) and metal chlorides/oxides (including $NiCl_2$ [25] and FeO [47]) are adopted to etch substrate of HCs. Subsequently, the substrate loaded numerous defects can be created due to the hollow and loose framework [24, 48, 49]. Cobalt salt ramification (e.g., Co_3O_4), significantly, can form more homogenous nanoscale pores and numerous active sites in carbon to produce fast sodium-ion channels [50]. In addition, Co_3O_4 is also proposed as a promising potential candidate anodic host material for SIBs [28]. In view of these advantages, temperature-control and pore-forming strategies will open up a novel way to fabricate high-performance carbonaceous anodes for rechargeable SIBs.

In this present work, we illuminate the transformation rules of defect/void ratio which affect the plateau/slope capacity. Moreover, the constraint relationship between specific capacity and rate capability is also explained. Inspired by this correlativity, porous hard carbon/Co_3O_4 particles (PHC/Co_3O_4) are prepared via the temperature-control carbonization (to achieve the optimal structure) and the pore-forming strategy (to build fast ion channels and ameliorate the retention ratio at high rate). Owing to the optimal defect/void ratio and fast ion channels, the PHC/Co_3O_4 anode exhibits excellent sodium-ion insertion/extraction performance with high reversible capacity, prolonged cyclic ability, and enhanced capacity at high rate. Our research proposes a synthetic method for preparation of economic carbonaceous anode for SIBs based on the sodium storage mechanism.

2. Results and Discussion

Platan tree plays an important role in building a beautiful urban environment in most cities. The fluffy catkins of platan fruit act as a raw material of HC due to its natural abundance and renewability. Cutting the platan fruit to fructus, plenty of fluffy catkins with diameters of 4 cm closely grown on the hard core (1.85 cm) can be seen (Figure S1). Additionally, the fluffy catkins possess a tubular structure with circular radius of 15-20 μm and the tube wall is 1.5 μm in the enlarged drawing. Figure 1 illuminates the transformation from fluffy catkins to PHC/Co_3O_4. There are two processing steps: temperature-control pyrolysis and pore-forming reaction.

2.1. Temperature-Control Pyrolysis. The ratio of defects and voids in HCs is adjusted by a simple pyrolysis process from 600°C to 1600°C (namely, HC600 to HC1600). With increasing the temperature, the graphitization degree of HCs is enhanced. Graphitization means the reduction of defects and the formation of voids. X-ray diffraction (XRD) and Raman spectra are used to characterize the interior structure of HCs (Figures 2(a) and 2(b)). There are two broad peaks at around 24° and 43° in XRD patterns. These two broad peaks refer to (002) and (101) diffraction arrangements and indicate the dominating amorphous structure in HCs (JCPDS 75-1621). Noticeably, the (002) peaks shift to higher angle slightly from 600°C to 1600°C due to the increase of graphitization as the defect-dominated arrangement. Some impurity peak of HC600 is ascribed to the incomplete pyrolysis. Moreover, the Raman spectra exhibit two characteristic bands. The differences in Raman spectra among HCs are attributed to the transformation of graphitic degree. As shown in Figure 2(b), D band (~1340 cm^{-1}) and G band (~1590 cm^{-1}) are manifest and the values of I_D/I_G are 3.85, 2.86, 2.56, 1.85, 1.45, and 1.22 corresponding to the different pyrogenic temperatures. The decrease of values (I_D/I_G) indicates the growth of atomic configuration.

Cyclic voltammetry (CV) tests in the first 5 cycles of all HCs are carried out at a specific scanning speed (0.1 mV s^{-1}). All the HCs exhibit the distinct oxidation peak in the first cycle due to the formation of solid electrolyte interface (SEI) (Figure S2). HC600 exhibits differentiated curves due to the incomplete carbonization. Beyond that, the other HCs synthesized at different pyrolysis temperature show similar CV curves: all samples exhibit an obvious redox peak at around 0.5 V. To further display the specific capacity change for all HCs treated at different temperature, the CV curves of all HCs in 5th cycle are summarized in Figure S3. It is obvious that the interior area raises from HC600 to HC1200 and

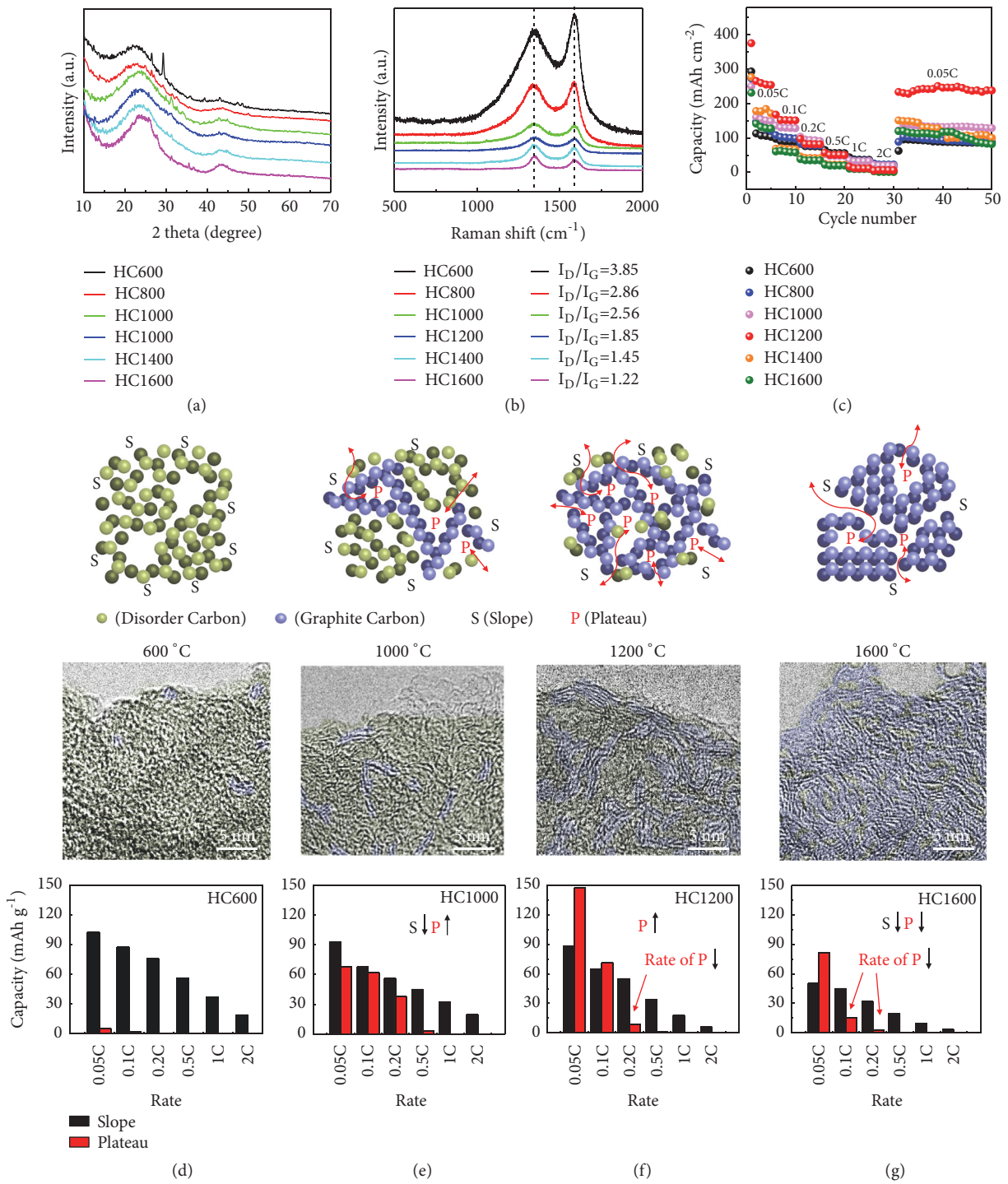


FIGURE 2: (a) XRD patterns and (b) Raman spectra of HCs. (c) Rate performance of HCs (1 C=300 mA g^{-1}). The transformation mechanism of defects/voids and specific slope/plateau capacities of HCs treated at (d) 600°C, (e) 1000°C, (f) 1200°C, and (g) 1600°C.

decreases to HC1600 subsequently. Consequently, HC1200 shows the largest CV curve area among all HCs, suggesting the largest specific capacity.

Rate and cycling performances of all HCs are evaluated using half-cells (Figures 2(c) and S4). HC1200 shows the highest specific capacity in cyclic performance test. However, the sodium storage behaviors of HC1200 are not perfect, especially the rate capability. To further clarify the capacity change mechanism, the galvanostatic discharge/charge profiles are analyzed at different rates (Figure S5). All the HCs display similar voltage profiles comprising a sloping segment (high voltage) and a plateau segment (low voltage). According to absorption-filling mechanism, the slope and plateau capacities are corresponding to the sodium storage

performance of defects and voids, respectively. Brunauer-Emmett-Teller (BET) results are conducted to prove the assumption. Figure S6 shows the pore size distribution of HCs (from HC800 to HC1400). The specific surface area and the number of pores decrease with the increase of carbonization temperature, indicating the decrease of defects. This is owing to the increase in graphitic degree and the agglomeration of pores in graphite layers.

The change rule of slope and plateau capacity of all the HCs is presented clearly in Figures 2(d)–2(g). HC600 is full of defects and a few voids (Figure 2(d)), which exhibits a high slope capacity and low plateau capacity. With the increase of pyrolysis temperature, the voids in HC1000 increase significantly and the defects decrease slightly due to the cross-pile-up of graphitization carbon (Figure 2(e)), whereas too high degree of graphitization for HCs will cause orderly-pile-up of graphitization carbon, resulting in significant reduction of voids and ion channels. This process is presented by the high-resolution TEM (HRTEM) images vividly (Figures 2(d)–2(g) and S7). The graphite layers are short and disordered when carbonized at low temperature. The chaotic layers will elongate and arrange in order when the carbonized temperature increases. Variation of capacity is caused by the change of structure. As shown in Figure 2(g), both the slope and plateau capacities of HC1600 decrease. Moreover, the initial Coulombic efficiencies are shown in Figure S8. Figure S9 summarizes the variation of plateau/slope capacity. Therefore, it is concluded that (a) the high capacity anode with excellent rate performance due to the interinhibitive relationship between defects and voids is hard to acquire and (b) optimal pyrolysis temperature will help in achieving the high volume of voids and optimizing the ratio of slope and plateau capacities. Taking all these factors into consideration, HCs cannot be acquired simultaneously without further modification.

2.2. Pore-Forming Reaction. HC1200, the highest capacity sample, shows a poor rate performance (Figure 2(f)). Inspired by the mechanism discussed above, the pore-forming strategy can open the fast transfer channels for sodium ions and break the bottleneck of capacity. The pore-forming process is also illustrated in Figure 1. HCs are immersed in $Co(CH_3COO)_2$ solution and heated at 400°C in air to form a porous structure. The surface of HCs is confronted with a corrosion process [51]. The specific corrosion process is illustrated as follows:

$$Co\left(CH_3COO\right)_2 + 2O_2 + C \xrightarrow{\text{heat}} \frac{1}{3}Co_3O_4 + \frac{4}{3}CO + \frac{2}{3}CO_2 + C_2H_4 \quad (1)$$

$$\frac{1}{3}Co_3O_4 + \frac{1}{3}C \xrightarrow{\text{heat}} \frac{1}{3}CO + CoO \quad (2)$$

$$CoO + \frac{1}{6}O_2 \xrightarrow{\text{heat}} \frac{1}{3}Co_3O_4 \quad (3)$$

$$\frac{4}{3}CO + \frac{2}{3}O_2 \xrightarrow{\text{heat}} \frac{4}{3}CO_2 \quad (4)$$

$$C_2H_4 + 3O_2 \xrightarrow{\text{heat}} 2CO_2 + 2H_2O \quad (5)$$

Carbon reacts with $Co(CH_3COO)_2$ and results in the formation of Co_3O_4 (see (1)). In this process, Co_3O_4 is the key material to form porous structure. Mutual conversion of Co_3O_4 and CoO consumes part of the carbon. During the heat treatment process, the chain reactions (see (2) and (3)) proceed continuously and porous carbon with abundant defects is prepared.

The SEM image of PHC/Co_3O_4 displays a rough surface, while HC1200 demonstrates a relatively smooth surface (Figures 3(a)-3(b)). The high-magnification SEM images (Figure 3(b) inset and Figure S10) present that the close-packed sags and crests are formed on the surface of tubular HCs after the reactions. Moreover, HRTEM images can display the graphitic layer. There are many disordered regions in PHC/Co_3O_4, and these regions are composed of curved parallel graphene layers (Figure 3(c)). Figure S10a displays carbon edges on the surface, which serve as important active sites for insertion and deintercalation of sodium ions. In addition, a HRTEM micrograph of porous carbon tube is shown in Figure S10b. The distances between two layers are 0.246 nm and 0.204 nm referring to the (311) and (400) crystal faces in Co_3O_4, respectively. Figures S10c-d show the TEM images of PHC. Compared with HC1200, the overall surface of PHC changes from "flatter" to "sags and crests". Besides, the energy dispersive spectrometer (EDS) is conducted to reveal the distribution of Co_3O_4 in PHC/Co_3O_4 (Figure 3(d)). The undertint outline refers to carbon substrate and white particles refer to Co_3O_4. C, Co, and O elements match well with the image, which offers new evidence for the homogenous distribution of Co_3O_4.

The microstructures of HC1200, PHC/Co_3O_4, and PHC are also analyzed by XRD and Raman spectroscopy. The XRD patterns illustrate the interior structure and ingredient (Figure 3(e)). Two broaden diffraction peaks located at 24° and 43° in the XRD patterns suggest the similar disordered and amorphous structure of three samples. Moreover, the distinct characteristic peaks of Co_3O_4 phase (JCPDS 01-1152) can be seen in the pattern of PHC/Co_3O_4. As shown in Figure 3(f), there are two broadened peaks in the same position with the same I_D/I_G value (1.85) for all samples in Raman spectra and an extra typical cobalt oxide peak at 675 cm^{-1} appears only in PHC/Co_3O_4. Thermogravimetric analysis (TGA) is conducted for testing the weight change of PHC/Co_3O_4 and HC1200 in air. Comparative thermograms of three samples are shown in Figure 3(g). The profile of PHC/Co_3O_4 has a higher residue after heating to 800°C revealing the Co_3O_4 content. A mass loss at low temperature (lower than 180°C) in both PHC/Co_3O_4 and PHC is attributed to the higher moisture. The content of Co_3O_4 is measured by inductively coupled plasma-optical emission spectrometry (ICP). As shown in Table S1 and Figure S11, the content of Co_3O_4 is 18.11 wt.% in PHC/Co_3O_4. Correspondingly, the measured Co_3O_4 content in PHC is 0.01 wt.% which is negligible. From the XPS full spectra, obvious Co peaks only appear in PHC/Co_3O_4 (Figure S12). The Co 2p spectrum contains two oblique

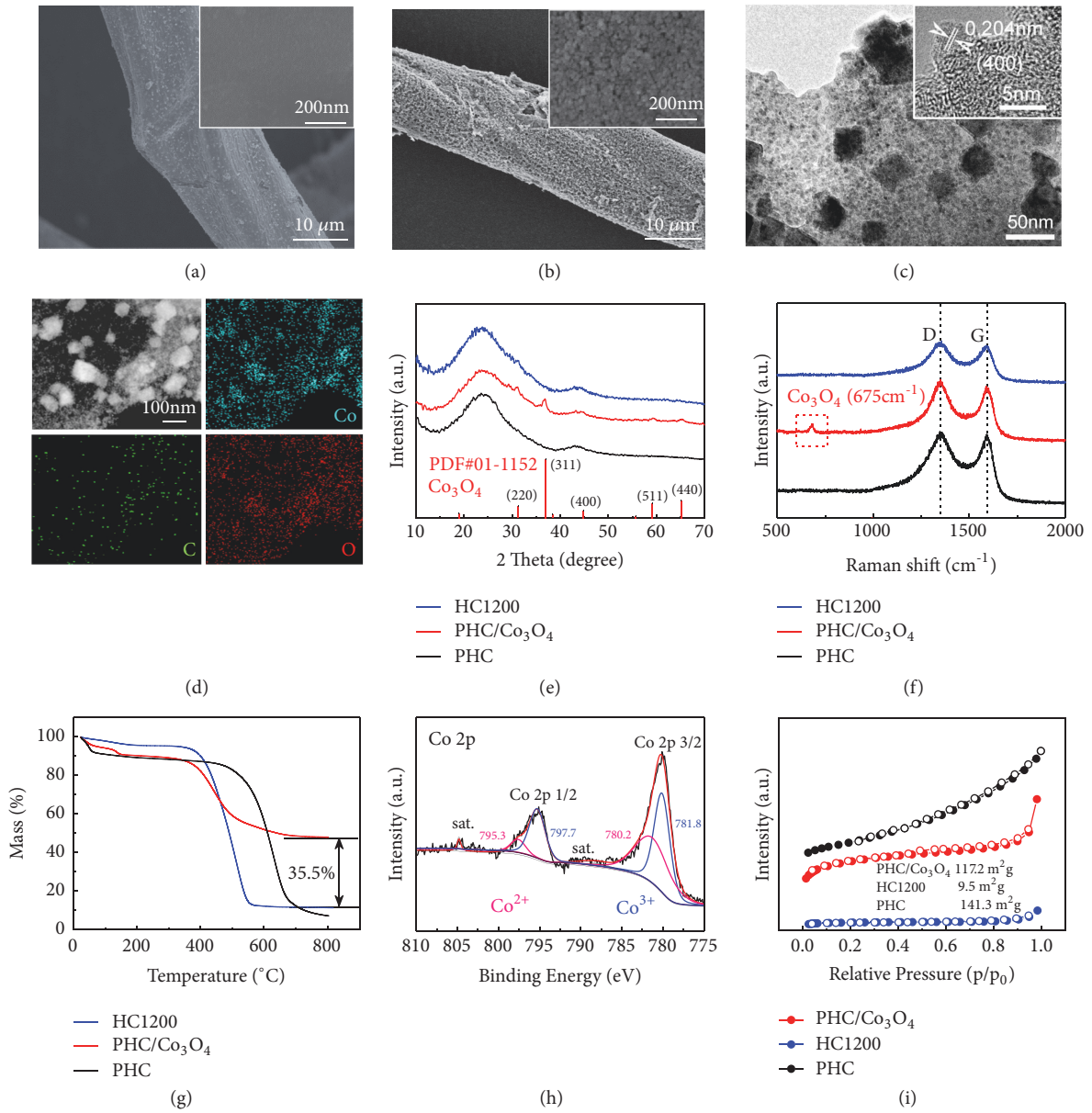


Figure 3: Characterization results of HC1200, PHC/Co_3O_4, and PHC. SEM images of (a) HC1200 and (b) PHC/Co_3O_4; (c) TEM images PHC/Co_3O_4; (d) EDS elemental mapping of PHC/Co_3O_4; (e) XRD patterns, (f) Raman spectra and (g) TG results of HC1200, PHC/Co_3O_4, and PHC; (h) XPS Co 2p spectrum of PHC/Co_3O_4. (i) Nitrogen adsorption/desorption isotherms of HC1200 and PHC/Co_3O_4.

$Co2p_{1/2}$ (795.3 eV and 797.7 eV) and $Co2p_{3/2}$ (780.2 eV and 781.8 eV) peaks revealing the presence of Co^{2+} and $C_O{}^{3+}$ (Figure 3(h)), corresponding to the cobalt oxide CoO and Co_2O_3 in Co_3O_4 [52]. To characterize the specific surface area of PHC/Co_3O_4, nitrogen adsorption/desorption isotherms are performed. As we expected, PHC/Co_3O_4 shows supernal pores and higher specific surface area (117.2 $m^2\ g^{-1}$) than HC1200 (9.5 $m^2\ g^{-1}$) (Figure 3(i)). In addition, PHC possesses a higher surface area than PHC/Co_3O_4 due to wiping off from Co_3O_4.

The sodium-ion storage properties of PHC/Co_3O_4, PHC, and HC1200 electrodes are evaluated via half-cells with 1 M $NaClO_4$ electrolyte. The CV curve of PHC/Co_3O_4 shows a little broader area, and the redox peak at 0.54 V refers to the overlap of Co_3O_4 and carbon redox peaks (Figure S13a). The CV curve at a low scan rate of 0.05 mV s^{-1} is shown in Figure S13c. The redox peaks of Co_3O_4 at about 1.6 V, 0.36 V, and 0.96 V can be identified [12, 53]. When Co_3O_4 is removed by HNO_3, the CV curve of PHC returns to the spiculate redox peak (Figure S13b). Figure 4(a) represents the rate performances of PHC/Co_3O_4, PHC, and HC1200 electrodes between 0.1 C and 5 C. Evidently, the PHC/Co_3O_4 electrode shows the highest capacity. The capacity of PHC/Co_3O_4 is about 100 mAh g^{-1} at 5 C, while HC1200 is less than 5 mAh g^{-1}. The highest capacity of PHC/Co_3O_4 is contributed to the synergistic of Co_3O_4 and rich-defect carbon. In addition,

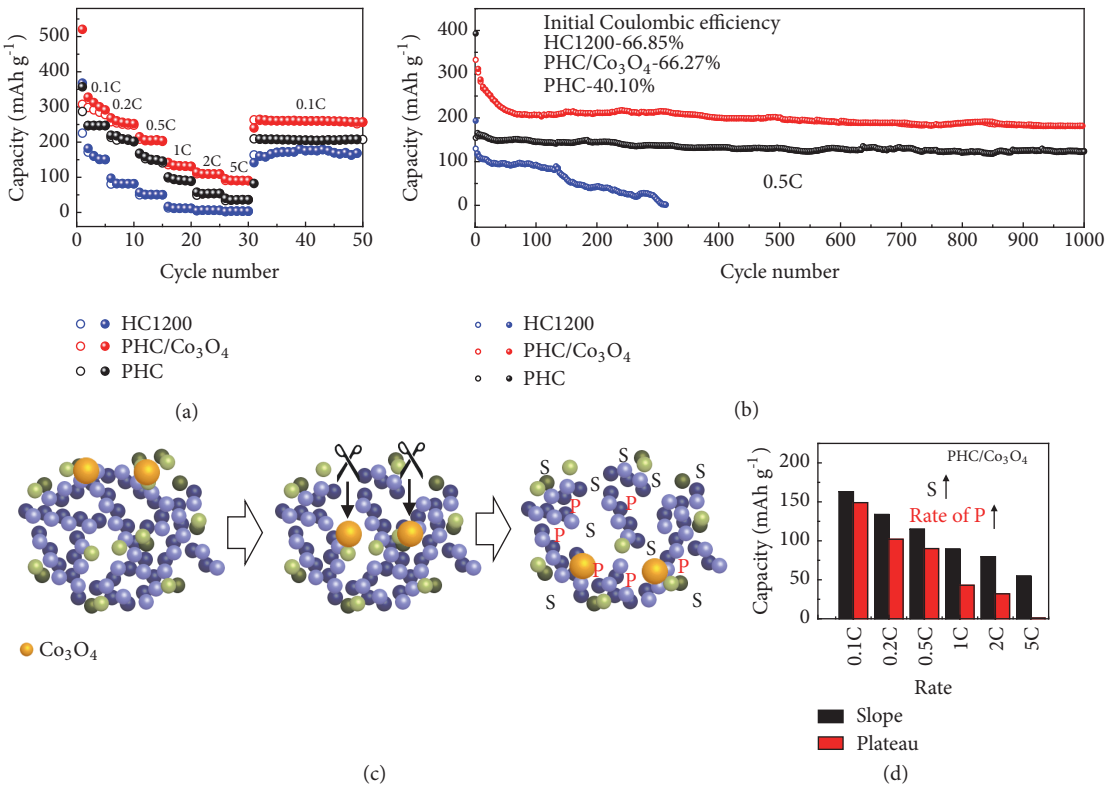


FIGURE 4: Electrochemical performance of the half-cells and the mechanism. (a) Rate performance and (b) cycling performance of HC1200, PHC/Co_3O_4, and PHC anodes. (c) The action mechanism of Co_3O_4 as catalyst to increase the slope and plateau capacity. (d) Slope and plateau capacities of PHC/C at different rates.

the initial Coulombic efficiency of PHC/Co_3O_4 (66.27%) is similar to HC1200. Figure 4(b) exhibits the long cycling results of three samples. The PHC/Co_3O_4 electrode preserves a high capacity (200 mAh g^{-1}) that can remain stable (remain 87%) after 1000 cycles, superior to PHC (148 mAh g^{-1}) and HC1200 (serious capacity deterioration). Moreover, Co_3O_4 in PHC/Co_3O_4 (18.114 wt.%) can provide certain extra capacity and the synergistic effect of Co_3O_4 and PHC is also contributed to the enhanced capacity (details are shown in computation part in Supporting Information). In addition, the Coulombic efficiency of PHC/Co_3O_4 is over 99% during cycling (except for the first cycle). As a reference, pure commercial Co_3O_4 displays a serious capacity deterioration to about 5 mAh g^{-1} after only 4 cycles (Figure S14). Advantages of the designed porous structure of PHC/Co_3O_4 with enhanced electrochemical performance are emphasized here: (1) shorten the ion/electron transfer path which is favorable for high rate applications, (2) amplify the full-cell voltage because HC possesses a low and explanate redox potential, (3) accelerate the shuttle of electrolyte in the HC anode, and (4) enhance the slope capacity resulting from the presence of defects and edges.

The diagrams of the galvanostatic discharge/charge profiles at different rates are further analyzed to prove this hypothesis (Figure S15). Figure 4(c) describes the action mechanism of Co_3O_4 to increase the slope and plateau capacity. HC1200 presents the highest capacity due to the optimal plateau/slope ratio. The pore-forming reaction creates numerous defects (slope capacity), builds fast ion channels for the nanovoids (plateau capacity), and provides additional capacity by residual Co_3O_4. Figure 4(d) shows a clear capacity distribution in the slope and plateau capacities of PHC/Co_3O_4. Compared with HCs, the retentions of both slope and plateau capacities of PHC/Co_3O_4 at high rates are greatly enhanced via pore-forming strategy.

To further demonstrate its potential applications for SIBs, the PHC/Co_3O_4 anode is coupled with $Na(Ni_{0.8}Co_{0.1}Mn_{0.1})O_2$ (NNCM) cathode to assemble full cells. Figure 5(a) illustrates that the capacity of PHC/Co_3O_4//NNCM is over 100 mAh g^{-1} at a high rate of 5 C and can return back to almost the original capacity of around 270 mAh g^{-1} at a low rate of 0.1 C. Moreover, the charge/discharge curve of full cells is displayed in Figure S16. In addition, the PHC/Co_3O_4/NNCM cell delivers a stable and prolonged cycling performance as the specific capacity still retains about 83% after 1000 cycles (Figure 5(b)).

3. Conclusions and Outlook

In summary, we have illuminated the mechanism for high-performance PHC/Co_3O_4 anode via two processing steps: temperature-control pyrolysis and subsequent pore-forming reaction. Firstly, a relative high-performance hard carbon is successfully prepared by temperature-control pyrolysis.

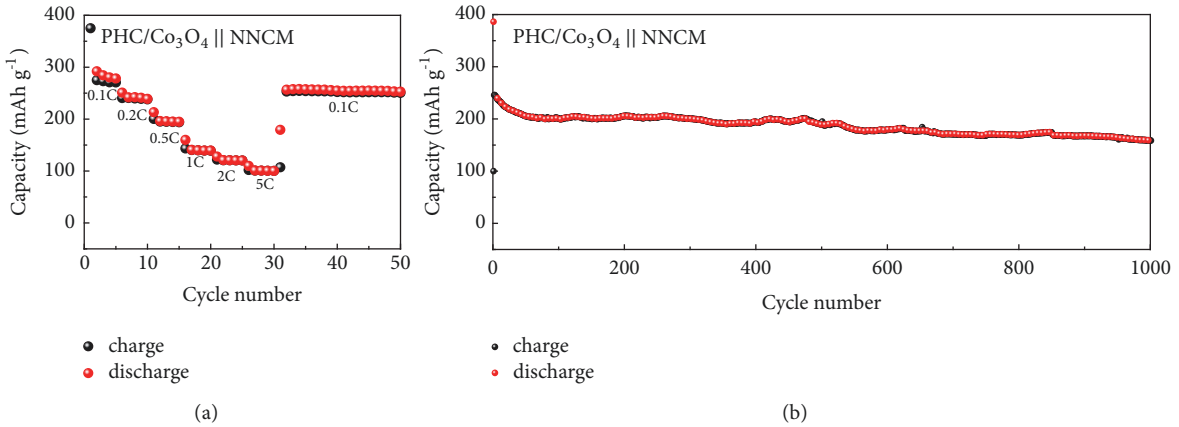


Figure 5: Electrochemical performance of PHC/Co_3O_4/NNCM full batteries. (a) Rate performance and (b) long cycling performance.

Then, PHC/Co_3O_4 is fabricated from the hard carbon via subsequent pore-forming reaction. The pore-forming reaction can create abundant defects and build fast sodium-ion channels to further greatly enhance both capacity and rate capability. Moreover, after the pore-forming process, the residual Co_3O_4 offers extra capacity due to the synergistic effect of PHC and Co_3O_4. Therefore, the PHC/Co_3O_4 anode exhibits a high capacity (270 mAh g^{-1}), enhanced capabilities at high rates, and prolonged cyclic stability. These consequences take into account the sodium-ion storage behavior from a new perspective and furthermore deepen the understanding of plateau/slope controllable carbonaceous anode for SIBs.

Disclosure

Yuqian Li and Liyuan Zhang are co-first authors.

Conflicts of Interest

The authors declare that they have no conflicts of interest.

Acknowledgments

This work is financially supported by the Ministry of Education's "Program for Innovative Research Team in University" (IRT13037), Qianjiang Talents Plan D (QJD1602029), Fundamental Research Funds for the Central Universities (2018QNA4011), the Postdoctoral Science Foundation of Zhejiang Province (zj20180111), and College Students Science and Technology Innovation Activity Plan of Zhejiang Province (2018R401251).

Supplementary Materials

Experimental Section: computational process of the specific capacity of Co_3O_4. Figure S1: (a) planetree fruit; (b) silk stripping from the threadlet; (c) cross section of planetree fruit; (d) optical enlargement of TCF. Figure S2: CV curves of HCs synthesized at (a) 600°C, (b) 800°C, (c) 1000°C, (d) 1200°C, (e) 1400°C, and (f) 1600°C at the first 5 cycles. Figure S3: CV curve of HCs between 0.01 and 2.5 V at a scan rate of 0.1 mV s^{-1} at 5th cycle. Figure S4: cycling performance of HCs at 0.1C. Figure S5: charging and discharging curves of HCs synthesized at (a) 600°C, (b) 800°C, (c) 1000°C, (d) 1200°C, (e) 1400°C, and (f) 1600°C at different rate. Figure S6: (a) micropore and (b) mesopore size distribution of HCs (HC800 to HC1400). Figure S7: HRTEM images of (a) HC600, (b) HC1000, (c) HC1200, and (d) HC1600. Figure S8: initial Coulombic efficiencies of HCs. Figure S9: capacity and plateau/slope ratio of all HCs. Figure S10: (a, b) TEM images of PHC/Co_3O_4; (c-d) TEM images of PHC. Table 1: the ICP signals of 200 ml HNO_3 solution (enough to dissolution Co_3O_4) immersed in 15 mg PHC/Co_3O_4 and PHC then taking out 20 ml filtered solution attenuation to 200 ml and the standard samples. Figure S11: the Co ion intensity signal images of PHC/Co_3O_4, PHC, and standard sample attenuation solutions tested by ICP. Figure S12: XPS full spectra of HC1200, PHC/Co_3O_4, and PHC. Figure S13: CV curves of (a) PHC/Co_3O_4 and (b) PHC; (c) PHC/Co_3O_4 at a low scan rate of 0.05 mV s^{-1}. Figure S14: rate and cycling performances of pure Co_3O_4. Figure S15: charging and discharging curves of PHC/Co_3O_4 (a) and PHC (b) at different rate. Figure S16: the charge/discharge curve of full cells. *(Supplementary Materials)*

References

[1] V. Etacheri, R. Marom, R. Elazari, G. Salitra, and D. Aurbach, "Challenges in the development of advanced Li-ion batteries: a review," *Energy & Environmental Science*, vol. 4, no. 9, pp. 3243–3262, 2011.

[2] X. Tao, K. Wang, H. Wang et al., "Controllable synthesis and in situ TEM study of lithiation mechanism of high performance NaV_3O_8 cathodes," *Journal of Materials Chemistry A*, vol. 3, no. 6, pp. 3044–3050, 2015.

[3] M. D. Slater, D. Kim, E. Lee, and C. S. Johnson, "Sodium-ion batteries," *Advanced Functional Materials*, vol. 23, no. 8, pp. 947–958, 2013.

[4] J. Shi, D. Xiao, M. Ge et al., "High-capacity cathode material with high voltage for Li-ion batteries," *Advanced Materials*, vol. 30, no. 9, Article ID 1705575, 2018.

[5] L. Zhang, H. Huang, H. Yin et al., "Sulfur synchronously electrodeposited onto exfoliated graphene sheets as a cathode material for advanced lithium–sulfur batteries," *Journal of Materials Chemistry A*, vol. 3, no. 32, pp. 16513–16519, 2015.

[6] D. Nam, T. Kim, K. Hong, and H. Kwon, "Template-free electrochemical synthesis of Sn nanofibers as high-performance anode materials for Na-ion batteries," *ACS Nano*, vol. 8, no. 11, pp. 11824–11835, 2014.

[7] C. Yue, Y. Yu, S. Sun et al., "High performance 3D Si/Ge nanorods array anode buffered by TiN/Ti interlayer for sodium-ion batteries," *Advanced Functional Materials*, vol. 25, no. 9, pp. 1386–1392, 2015.

[8] J. Ni, S. Fu, C. Wu et al., "Superior sodium storage in $Na_2Ti_3O_7$ nanotube arrays through surface engineering," *Advanced Energy Materials*, vol. 6, no. 11, Article ID 1502568, 2016.

[9] X. Ding, X. Huang, J. Jin, H. Ming, L. Wang, and J. Ming, "Sustainable solid-state strategy to hierarchical core-shell structured Fe_3O_4@graphene towards a safer and green sodium ion full battery," *Electrochimica Acta*, vol. 260, pp. 882–889, 2018.

[10] Y. Zhu, X. Han, Y. Xu et al., "Electrospun Sb/C fibers for a stable and fast sodium-ion battery anode," *ACS Nano*, vol. 7, no. 7, pp. 6378–6386, 2013.

[11] H. Huang, L. Zhang, Y. Xia et al., "Well-dispersed ultrafine Mn_3O_4 nanocrystals on reduced graphene oxide with high electrochemical Li-storage performance," *New Journal of Chemistry*, vol. 38, no. 10, pp. 4743–4747, 2014.

[12] Y. Liu, Z. Cheng, H. Sun, H. Arandiyan, J. Li, and M. Ahmad, "Mesoporous Co_3O_4 sheets/3D graphene networks nanohybrids for high-performance sodium-ion battery anode," *Journal of Power Sources*, vol. 273, pp. 878–884, 2015.

[13] M. Xu, Q. Xia, J. Yue et al., "Rambutan-like hybrid hollow spheres of carbon confined Co_3O_4 nanoparticles as advanced anode materials for sodium-ion batteries," *Advanced Functional Materials*, vol. 29, no. 6, Article ID 1807377, 2019.

[14] X. Ao, J. Jiang, Y. Ruan et al., "Honeycomb-inspired design of ultrafine SnO_2@C nanospheres embedded in carbon film as anode materials for high performance lithium-and sodium-ion battery," *Journal of Power Sources*, vol. 359, pp. 340–348, 2017.

[15] Y. Tang, Z. Zhao, X. Hao et al., "Engineering hollow polyhedrons structured from carbon-coated $CoSe_2$ nanospheres bridged by CNTs with boosted sodium storage performance," *Journal of Materials Chemistry A*, vol. 5, no. 26, pp. 13591–13600, 2017.

[16] L. Yu, J. F. Yang, and X. W. D. Lou, "Formation of CoS_2 nanobubble hollow prisms for highly reversible lithium storage," *Angewandte Chemie International Edition*, vol. 55, no. 43, pp. 13422–13426, 2016.

[17] G. Wang, J. Zhang, S. Yang et al., "Vertically aligned MoS_2 nanosheets patterned on electrochemically exfoliated graphene for high-performance lithium and sodium storage," *Advanced Energy Materials*, vol. 8, no. 8, Article ID 1702254, 2018.

[18] D. Xie, X. Xia, W. Tang et al., "Novel carbon channels from loofah sponge for construction of metal sulfide/carbon composites with robust electrochemical energy storage," *Journal of Materials Chemistry A*, vol. 5, no. 16, pp. 7578–7585, 2017.

[19] W. Tang, X. Wang, Y. Zhong et al., "Hierarchical MoS_2/carbon composite microspheres as advanced anodes for lithium/sodium ion batteries," *Chemistry - A European Journal*, vol. 24, no. 43, pp. 11220–11226, 2018.

[20] J. Qian, Y. Xiong, Y. Cao, X. Ai, and H. Yang, "Synergistic Na-storage reactions in Sn_4P_3 as a high-capacity, cycle-stable anode of Na-ion batteries," *Nano Letters*, vol. 14, no. 4, pp. 1865–1869, 2014.

[21] D. P. DiVincenzo and E. J. Mele, "Cohesion and structure in stage-1 graphite intercalation compounds," *Physical Review B: Condensed Matter and Materials Physics*, vol. 32, no. 4, pp. 2538–2553, 1985.

[22] G. Yoon, H. Kim, I. Park, and K. Kang, "Conditions for reversible Na intercalation in graphite: theoretical studies on the interplay among guest ions, solvent, and graphite host," *Advanced Energy Materials*, vol. 7, no. 2, Article ID 1601519, 2017.

[23] J. Yang, Z. Ju, Y. Jiang et al., "Enhanced capacity and rate capability of nitrogen/oxygen dual-doped hard carbon in capacitive potassium-ion storage," *Advanced Materials*, vol. 30, no. 4, Article ID 1700104, 2018.

[24] Z. H. Sun, J. Q. Zhang, L. C. Yin et al., "Conductive porous vanadium nitride/graphene composite as chemical anchor of polysulfides for lithium-sulfur batteries," *Nature Communications*, vol. 8, p. 14627, 2017.

[25] Y. Zhong, X. Xia, S. Deng et al., "Popcorn inspired porous macrocellular carbon: rapid puffing fabrication from rice and its applications in lithium–sulfur batteries," *Advanced Energy Materials*, vol. 8, no. 1, Article ID 1701110, 2018.

[26] E. M. Lotfabad, J. Ding, K. Cui et al., "High-density sodium and lithium ion battery anodes from banana peels," *ACS Nano*, vol. 8, no. 7, pp. 7115–7129, 2014.

[27] K. Hong, L. Qie, R. Zeng et al., "Biomass derived hard carbon used as a high performance anode material for sodium ion batteries," *Journal of Materials Chemistry A*, vol. 2, no. 32, p. 12733, 2014.

[28] H. Li, Z. Li, X. Wu et al., "Shale-like Co_3O_4 for high performance lithium/sodium ion batteries," *Journal of Materials Chemistry A*, vol. 4, no. 21, pp. 8242–8248, 2016.

[29] T. Zhang, J. Chen, B. Yang, H. Li, S. Lei, and X. Ding, "Enhanced capacities of carbon nanosheets derived from functionalized bacterial cellulose as anodes for sodium ion batteries," *RSC Advances*, vol. 7, no. 79, pp. 50336–50342, 2017.

[30] P. Liu, Y. Li, Y. Hu, H. Li, L. Chen, and X. Huang, "A waste biomass derived hard carbon as a high-performance anode material for sodium-ion batteries," *Journal of Materials Chemistry A*, vol. 4, no. 34, pp. 13046–13052, 2016.

[31] Y. Li, Y. Hu, H. Li, L. Chen, and X. Huang, "A superior low-cost amorphous carbon anode made from pitch and lignin for sodium-ion batteries," *Journal of Materials Chemistry A*, vol. 4, no. 1, pp. 96–104, 2016.

[32] J. Luo, C. Fang, C. Jin et al., "Tunable pseudocapacitance storage of MXene by cation pillaring for high performance sodium-ion capacitors," *Journal of Materials Chemistry A*, vol. 6, no. 17, pp. 7794–7806, 2018.

[33] W. Li, R. Fang, Y. Xia et al., "Multiscale porous carbon aanomaterials for applications in advanced rechargeable batteries," *Batteries & Supercaps*, vol. 2, pp. 9–36, 2018.

[34] P. Lu, Y. Sun, H. Xiang, X. Liang, and Y. Yu, "3D amorphous carbon with controlled porous and disordered structures as a high-rate anode material for sodium-ion batteries," *Advanced Energy Materials*, vol. 8, no. 8, Article ID 1702434, 2018.

[35] J. Zhao, L. Zhao, K. Chihara et al., "Electrochemical and thermal properties of hard carbon-type anodes for Na-ion batteries," *Journal of Power Sources*, vol. 244, pp. 752–757, 2013.

[36] Y. Lu, C. Zhao, X. Qi et al., "Pre-oxidation-tuned microstructures of carbon anodes derived from pitch for enhancing Na storage performance," *Advanced Energy Materials*, vol. 8, no. 27, Article ID 1800108, 2018.

[37] Y. Qi, Y. Lu, F. Ding et al., "Slope-dominated carbon anode with high specific capacity and superior rate capability for high safety Na-ion batteries," *Angewandte Chemie*, vol. 131, no. 13, pp. 4405–4409, 2019.

[38] C. Zhao, Q. Wang, Y. Lu, B. Li, L. Chen, and Y. Hu, "High-temperature treatment induced carbon anode with ultrahigh Na storage capacity at low-voltage plateau," *Chinese Science Bulletin*, vol. 63, no. 17, pp. 1125–1129, 2018.

[39] J. Ding, H. Wang, Z. Li et al., "Carbon nanosheet frameworks derived from peat moss as high performance sodium ion battery anodes," *ACS Nano*, vol. 7, no. 12, pp. 11004–11015, 2013.

[40] L. Qie, W. Chen, X. Xiong et al., "Sulfur-doped carbon with enlarged interlayer distance as a high-performance anode material for sodium-ion batteries," *Advanced Science*, vol. 2, no. 12, Article ID 1500195, 2015.

[41] W. Wang, B. Jiang, L. Hu, Z. Lin, J. Hou, and S. Jiao, "Single crystalline VO_2 nanosheets: A cathode material for sodium-ion batteries with high rate cycling performance," *Journal of Power Sources*, vol. 250, pp. 181–187, 2014.

[42] C. Bommier, T. W. Surta, M. Dolgos, and X. Ji, "New mechanistic insights on Na-ion storage in nongraphitizable carbon," *Nano Letters*, vol. 15, no. 9, pp. 5888–5892, 2015.

[43] Y. Li, S. Xu, X. Wu et al., "Amorphous monodispersed hard carbon micro-spherules derived from biomass as a high performance negative electrode material for sodium-ion batteries," *Journal of Materials Chemistry A*, vol. 3, no. 1, pp. 71–77, 2015.

[44] P. Bai, Y. He, X. Zou, X. Zhao, P. Xiong, and Y. Xu, "Elucidation of the sodium-storage mechanism in hard carbons," *Advanced Energy Materials*, vol. 8, no. 15, Article ID 1703217, 2018.

[45] M. Pfiffer, P. Cormont, E. Fargin et al., "Effects of deep wet etching in HF/HNO_3 and KOH solutions on the laser damage resistance and surface quality of fused silica optics at 351 nm," *Optics Express*, vol. 25, no. 5, p. 4607, 2017.

[46] Y. You, W. Zeng, Y. Yin et al., "Hierarchically micro/mesoporous activated graphene with a large surface area for high sulfur loading in Li-S batteries," *Journal of Materials Chemistry A*, vol. 3, no. 9, pp. 4799–4802, 2015.

[47] L. Wang, J. Yu, X. Dong et al., "Three-dimensional macroporous carbon/Fe_3O_4-doped porous carbon nanorods for high-performance supercapacitor," *ACS Sustainable Chemistry & Engineering*, vol. 4, no. 3, pp. 1531–1537, 2016.

[48] L. Qie, W.-M. Chen, Z.-H. Wang et al., "Nitrogen-doped porous carbon nanofiber webs as anodes for lithium ion batteries with a superhigh capacity and rate capability," *Advanced Materials*, vol. 24, no. 15, pp. 2047–2050, 2012.

[49] X. Zhang, G. Zhu, M. Wang, J. Li, T. Lu, and L. Pan, "Covalent-organic-frameworks derived N-doped porous carbon materials as anode for superior long-life cycling lithium and sodium ion batteries," *Carbon*, vol. 116, pp. 686–694, 2017.

[50] D. Bin, X. Lin, Y. Sun et al., "Engineering hollow carbon architecture for high-performance K-ion battery anode," *Journal of the American Chemical Society*, vol. 140, no. 23, pp. 7127–7134, 2018.

[51] S. Abbas, H. Lee, J. Hwang et al., "A novel approach for forming carbon nanorods on the surface of carbon felt electrode by catalytic etching for high-performance vanadium redox flow battery," *Carbon*, vol. 128, pp. 31–37, 2018.

[52] L. Armelao, D. Barreca, S. Gross, and E. Tondello, "Sol-gel and CVD Co_3O_4 thin films characterized by XPS," *Surface Science Spectra*, vol. 8, no. 1, pp. 14–23, 2001.

[53] D. Xin, J. Dai, J. Liu, Q. Wang, and W. Li, "Mesocrystal hexagonal Co_3O_4 nanosheets for high performance lithium and sodium-ion batteries," *Materials Letters*, vol. 209, pp. 388–391, 2017.